

Article

Pluronic-123 Assisted Synthesis of Cobalt Vanadate Microparticles (μ -CoV MPs) for Durable Electrochemical Oxygen Evolution Reaction in Seawater and Connate Water

Ibrahim Khan [†] 

School of Chemical Engineering and Materials Science, Chung-Ang University, 84 Heukseok-ro, Dongjak-gu, Seoul 06974, Republic of Korea; ebraheem.chemist@gmail.com or ebraheemchem@cau.ac.kr

[†] Ibrahim Khan (BrainPool Researcher).

Abstract: Exploring different catalytic material paradigms could drive the search for the best oxygen evolution reaction (OER) catalyst to achieve industrially-feasible hydrogen fuel from water. Cobalt-based materials are considered good choices in this regard. Herein, we synthesized *Pluronic-123* (*P-123*)-stabilized, unique, rough, globular-shaped cobalt vanadate microparticles (μ -CoV MPs) using an ultrasonic-assisted solvothermal method. The as-synthesized μ -CoV MPs were subjected to high-temperature annealing to improve the crystallinity and the surface polymer moieties were pyrolyzed. Conventional SEM, XRD, FTIR, and BET analyses evaluated the morphological and structural features. The temperature-controlled crystalline phase led to extensive OER performance in SW electrolytes. The OER onset potential (V_{OER}) was observed at 1.557 V@10 mA/cm² in seawater (SW) for μ -CoV MPs annealed at 400 °C compared to the V_{OER} of 1.632 V of non-annealed μ -CoV MPs. The current density showed a steep increase beyond 1.557 V, confirming the excellent electrokinetics OER behavior of the μ -CoV MPs-deposited electrode. The chronoamperometric (*I-t*) OER stability comparison in SW and connate water (CW) electrolytes indicated only a <20% initial current density decrease after 8 h in the case of the SW electrolyte. However, the CW electrolyte posed serious challenges to the electrode and activity was completely lost after <2 h. The electrolytic comparison indicated that SW is highly suitable for μ -CoV MPs electrodes.



Citation: Khan, I. *Pluronic-123* Assisted Synthesis of Cobalt Vanadate Microparticles (μ -CoV MPs) for Durable Electrochemical Oxygen Evolution Reaction in Seawater and Connate Water. *Catalysts* **2023**, *13*, 636. <https://doi.org/10.3390/catal13030636>

Academic Editors: Tahir Muhmood, Xiaofei Yang and Jae Sung Lee

Received: 6 February 2023

Revised: 13 March 2023

Accepted: 20 March 2023

Published: 22 March 2023



Copyright: © 2023 by the author. Licensee MDPI, Basel, Switzerland. This article is an open access article distributed under the terms and conditions of the Creative Commons Attribution (CC BY) license (<https://creativecommons.org/licenses/by/4.0/>).

Keywords: cobalt vanadate (CoV); OER; water splitting; seawater; connate water; *Pluronic-123* (*P-123*)

1. Introduction

Alternative energy conversion/storage protocols have generated intense research interest in seeking potential electrode materials that are highly efficient, low cost and environmentally friendly. One such material under consideration is hydrogen, which has an ideal energy carrier capacity. Water is the best precursor to obtain hydrogen fuel [1–7]. In this regard, electrochemical water spitting (EC-WS) is a desirable option that could split water into two steps: (1) the oxygen evolution reaction (OER), which is an oxidation step involving the generation of oxygen by four-electron transfer and is highly complex, and (2) the hydrogen evolution reaction (HER), which is a reduction step involving the generation of hydrogen by two-electron transfer, and is relatively feasible [8]. Hence, the OER is the rate-determining step in water splitting, and further research into the fabrication of an OER catalyst is ongoing [9,10]. Moreover, the separation of hydrogen and oxygen can improve the water splitting efficiency of the device [11]. Noble and rare earth metals such as Pt, Ru, Ir, and their oxides have been found to have excellent OER performance, but their unavailability and cost are major concerns. During the last decade, cobalt-based materials have found new paradigms applicable to EC-WS [12–14]. These are cost-effective, environmentally friendly, abundantly available, thermally stable, and offer the feasibility of being modified structurally and morphologically by simple synthetic strategies. Their electrochemical properties in alkaline electrolytes are by far comparable with most of the

available industrial catalysts. For instance, conventional Co_3O_4 NPs, mesoporous Co_3O_4 NPs, and their composites with carbon materials (graphene, carbon black, carbon nitride, etc.), decorated metal and metal oxides NPs, functionalization by organic compounds, etc., have been reported to have substantial OER and HER applications [15–19]. The heterostructures of cobalt oxides by substituting Co with metals such as Mn, Ni, Cu, and Fe in the crystal lattice improve the OER performance of $\text{MnCo}_{2-x}\text{O}_4$, NiCo_xO_y , CuCo_xO_y and FeCo_xO_y catalysts compared to conventional Co_3O_4 NPs [20–25]. These cases suggested that forming binary metal oxides of Co could be one of the solutions to acquiring the best cobalt-based OER performance materials. In this regard, metal vanadates have been pursued in recent years due to their ease of preparation, cost-effectiveness, and better conductivities. Our group has thoroughly investigated bismuth vanadate, copper vanadate, zinc vanadate, and nickel vanadate and their composites for water-splitting applications [6,26–29]. These materials offered exceptional electrochemical conductivities and stabilities when applied as anodes during water-splitting applications.

In addition to materials, selecting an electrochemically and commercially suitable electrolyte is equally important for a better electrochemical outcome. Seawater (SW) and connate or formation water (CW) are naturally occurring electrolytes and offer a good paradigm to be applied in water splitting applications. Moreover, their capacity to maintain distinct charge gradients in the midst of electrolytes result in the phenomenon of diffusiophoresis (DP). DP is recognized as one of the mass transfer mechanisms and arises due to the existence of concentration gradients in the fluid's media without implying external energy input. Based on the nature of the electrolyte, DP could be electrolytic and non-electrolytic [30–32]. Soren et al. provided an early overview to deal with the challenges associated with SW oxidation [33]. Few reports have practically demonstrated SW water oxidation with great success, such as the efficacy of NiFe-LDH as a catalyst for the OER in SW compared to commercial IrOx-based catalysts in a specially designed asymmetric cell. Unlike IrOx, NiFe-LDH shows high selectivity for the OER in SW without causing the oxidation of Cl^- even at cell potentials above 3.0 V [34]. Similarly, more recently, the multilayered NiFe-CuCo LDH was also found to be useful in SW OER [35]. The nitrides also offered a significant paradigm for SW OER. A core-shell metal-nitride catalyst, consisting of NiFeN NPs and NiMoN nanorods on Ni foam, was found to be a durable OER catalyst for alkaline SW electrolysis [36]. However, high-concentration SW and CW electrolytes involve complex transfer mechanisms and the faster kinetics can lead to the instant deterioration of the electrode materials, which immensely inhibits the long-term electrode performance [37]. Therefore, further investigations of highly durable electrode materials can be helpful to utilize the commercial values of these electrolytes in practical applications due to their commercial values.

Nonetheless, transition metal-based catalysts should still be investigated further to achieve industrially feasible electrocatalysts that show resilience in highly alkaline SW and CW media [38]. The primary aim of the current study is to explore the potential of spherical-shaped microspheres of cobalt vanadate particles ($\mu\text{-CoV}$ MPs) with high crystallinity, durability, and defect-incubation properties for the OER application in SW and CW. This marks the first investigation on cobalt vanadate comprised anodes in SW and CW electrolytes. As reported, CoV exists within Kagome staircase geometry with inherited magnetic behavior. CoV materials are widely recognized as the preferred choice for use as anodes in Li batteries and as positrode materials in supercapacitor applications. The first report on cobalt vanadate ($\text{Co}_3\text{V}_2\text{O}_8$) as an OER catalyst in an alkaline medium was provided by Xing et al. in 2014 [39]. They synthesized $\text{Co}_3\text{V}_2\text{O}_8$ NPs by using the chemical coprecipitation technique with low crystallinity and mesoporosity and a large surface area. The current density of 10 mA/cm^2 afforded a marginally higher overpotential of 359 mV. The literature lacks studies to explain the total OER performance of $\mu\text{-CoV}$ MPs in a mixture of brines (SW and CW) and its mechanism. Therefore, this study will offer a tutorial on how readers can use these materials for future water-splitting applications.

2. Results and Discussion

2.1. Synthesis of μ -CoV MPs

A wide research literature survey indicated that the synthesis of conventional cobalt vanadate usually followed a three-step protocol, i.e., (1) synthesis of V_2O_5 , (2) synthesis of Co_3O_4 , and (3) chemically reacting V_2O_5 and Co_3O_4 to obtain the vanadate product [39,40]. The multi-step process is usually time-consuming and poses many risks of adding impurities to the final product. Moreover, the structural and morphological control of the final product was hindered enormously. Therefore, herein, we have chosen an in situ approach to directly obtain the μ -CoV MPs product in a single reaction. For this purpose, we have adopted the synthetic protocol scheme in Figure 1a, which is loosely adapted from our previous reports on copper, nickel, bismuth, and zinc vanadates [26–28]. In the simple experiment, the calculated amount of NH_4VO_3 and $Co(NO_3)_2 \cdot 6H_2O$ hydrated metal salt was taken in the respective beakers in 50 mL absolute ethanol solvent (the synthesis scheme and quantities are provided in Figure 1a). The quantities of the precursors were adjusted based on the cobalt and vanadium metals ratio, as given in Table 1, with different reaction conditions. Many attempts were made to adjust the amount of *P-123* surfactant to achieve distinct morphology. The optimized *P-123* wt.% quantity is necessary to form micelles in the reaction mixture under given reaction conditions, which provide small reaction chambers for stabilizing the precursors' seed particles and condensing into microstructures particles (MPs) (schematic demonstration in Figure 1b) [6,41,42]. It was realized that 5 times *P-123* of the total weight of reactants has a significant impact on morphology control. The mixture was further subjected to pulse sonication for 30 min using an ultra/probe Sonicator (SONICS-4000 Vibra-Cell, Sonics & Materials, Inc. Newtown, CT, USA) operated at 20% amplitude at 50 °C. The pulses were provided at 10 s ON and 3 s OFF cycles. After ultrasonic probe treatment, the solution was transferred to a sealed Teflon-lined autoclave (OPTION INSTRUMENT CO., LIMITED, Shanghai China.) and kept at 120 °C for 12 h. Finally, the sample was washed several times to remove any unwanted impurities or untreated salts and allowed to dry. The final μ -CoV MPs product was subjected to calcination at various temperatures ranging from 100 to 800 °C. However, we found that above 400 °C, the μ -CoV MPs product sustained distinct morphology and crystallinity.

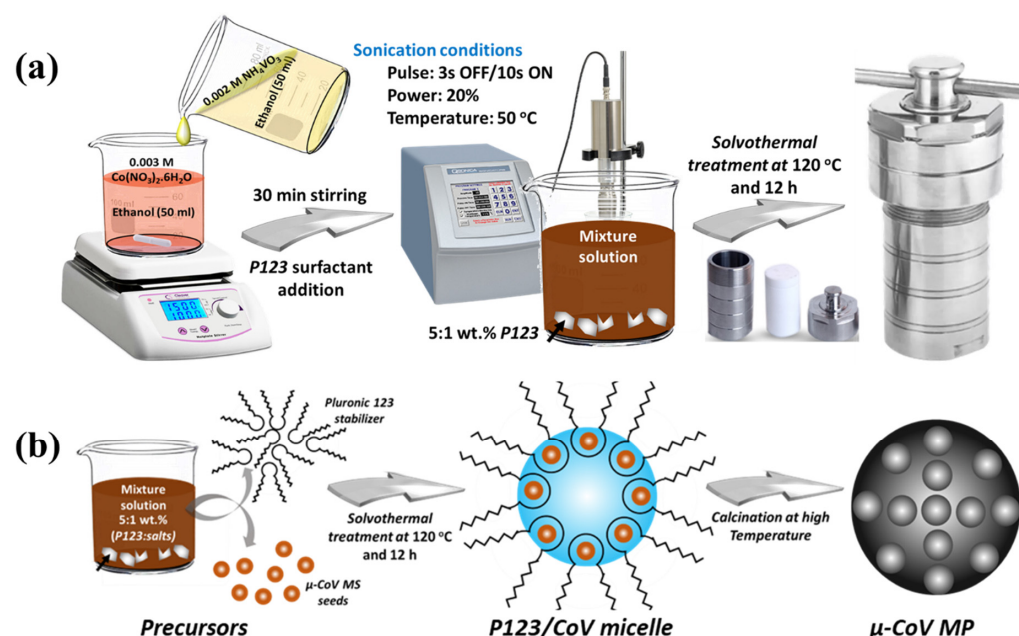


Figure 1. Synthetic scheme to obtain μ -CoV MPs using nitrate and vanadate precursors (a) The steps involved to obtain in situ μ -CoV MPs. (b) The mechanism of stabilization of μ -CoV MPs seeds into a microsize particle. The calcination at high temperatures leads to carbon content accumulation from the *P-123* polymer.

Table 1. Reaction conditions used for the preparation of various types of metal vanadates.

Type of Metal Vanadate	The Weight Ratio of Cobalt:Vanadium Precursors	Surfactant to Metal Precursor Weight Ratio	Reaction Temperature and Time	Physical Appearance
Co ₃ (VO ₄) ₂ (μ -CoV MPs)	3:2	1:5	120 °C for 12 h	Brown @ <200 °C Black @ >200 °C

2.1.1. Role of Ultrasonication in μ -CoV MPs Synthesis

Ultrasonication was an important step in the synthetic protocol since it provided the required energy necessary for the homogenous dispersion of the vanadate and metal precursor ions within the reaction media [29,43,44]. The high-energy ultrasonic waves caused cavitation due to their high energy, which is the most critical step in ultrasonication. Due to this phenomenon in the reaction medium, the growth and implosive collapse of microbubbles took place, which released high energy and generated localized hotspot regions. These hotspot regions could produce temperature and pressure up to 5000 K and 1000 bar, respectively [45,46]. The high-energy thermodynamics lead to desired transformation and dispersion of the agglomerated particles in the fluid matrix. Optimization of ultrasonic intensity, duration, external temperature, and pressure are equally important for sufficient output. If the process is standardized, it could lead to proper seed formation, which can be grown into distinct particles with desired shapes and crystallinities. In our case, the standardized conditions were found at 20% amplitude ultrasonic intensity, with 30 min of treatment at 50 °C.

2.1.2. Role of Pluronic (*P-123*) Surfactant in μ -CoV MPs Synthesis

Tri block poly(ethylene oxide)-poly(propylene oxide)-poly(ethylene oxide) (PEO-PPO-PEO) copolymer is a commercially available amphiphilic dispersion stabilizer in the form of Pluronic (*P-123*). It is widely used to synthesize various mesoporous nanoparticle materials. This material is useful to be used at a lower temperature, as it is hydrophilic at room temperature and changes its behavior at a higher temperature to hydrophobic [47]. *P-123* can successfully form vesicles/micelles, the internal size of which can range from a nanometer to a micrometer based on the reaction medium conditions. Highly stabilized *P-123* vesicles are important to attain desirable morphology and particle size. The Pluronic-assisted metal vanadate synthesis normally followed a similar pattern to a typical hydrothermal ripening process. The schematic presentation of the μ -CoV MPs seeds ripening process is provided in Figure 1b. As mentioned earlier, pulse sonication allows the precursor ions to react at the homogenous level. In the beginning, due to the electrostatic interactions, Co²⁺ metal ions attach to the terminal hydroxy groups (–OH) of the hydrophilic part of the surfactant. Meanwhile, highly dispersed VO^{3–} ions slowly interact with Co²⁺ ions, as they have comparatively slow diffusion due to their larger size and high steric hindrance [48]. The vanadate ion completely holds the metal ion and, therefore, is released by the surfactant at a high temperature during the hydrothermal treatment. With the provided time, the seeds grow into a particle of distinct shape with characteristic crystallinity. The surfactant is recovered at a high temperature; as we mentioned above, it became hydrophobic at a high temperature. The role of the surface is crucial to maintain the stepwise generation of seed particles, which develop into larger particles later. Without surfactants, we would not be able to attain specific morphology due to irregular and uncontrolled reactions between the metal and vanadate ions.

2.1.3. Role of Calcination Temperature in μ -CoV MPs Synthesis

The calcination temperature critically impacts the overall crystallinity, particle size, and morphology of the final product [6,49]. While optimizing the synthetic parameters, we tried different calcination temperatures, i.e., 200, 400 and 600 °C. However, we found that 400 °C and 600 °C are desirable temperatures, where the reported μ -CoV MPs existed in the most stable form with distinct morphology as also confirmed by the XRD spectra and SEM analyses.

We also believe that the carbonization of *P-123* surfactant occurred at high temperatures as the physical appearance of μ -CoV MPs appeared to be a black color from brown.

2.2. Morphological and Structural Confirmation of μ -CoV MPs

The main purpose of the protocol development is to achieve high crystallinity and distinct morphology, which could be helpful for respective applications. As dictated in the SEM images in Figure 2a,b, the μ -CoV MPs have distinct morphology. The highly agglomerated μ -CoV MPs seeds can be observed in the magnified SEM image in Figure 2b. We can assume that the smaller CoV seed particles have very high surface energies and to achieve stability they agglomerated into a large spherical ball-like shape (2–3 μm). The average sizes of small nanoballs seeds ranged from 100 to 200 nm. The same phenomenon was observed during the synthesis of pseudo flower-shaped BiVO_4 microarrays, where an SDS surfactant was used to control the morphology [29]. Similarly, other groups also reported the formation of metal oxide microparticles while using surfactant-assisted wet chemistry techniques and controlling the particle size by annealing at high temperatures [50–53].

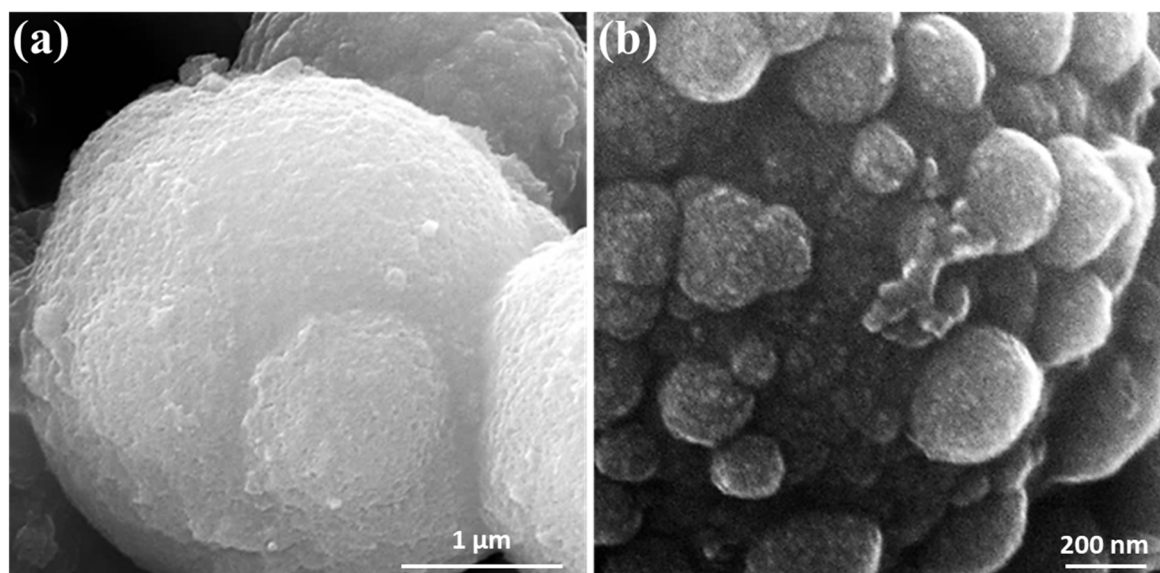


Figure 2. (a,b) Low and high-resolution FESEM of μ -CoV MPs. The high-resolution SEM indicates clear fused particles within the matrix.

2.3. XRD Patterns of μ -CoV MPs

To further illustrate the crystalline characteristics, we carried out the powder X-ray diffraction (PXRD) analysis of calcinated μ -CoV MPs samples, and the corresponding patterns are provided with respective labelling in Figure 3a. It can be clearly seen that the as-synthesized (uncalcined) μ -CoV MPs have poor crystallinity. The characteristic XRD peaks, i.e., (300), (400) and (440), were observed with low intensities. However, with the calcination temperature increase up to 600 $^{\circ}\text{C}$, μ -CoV MPs crystallinity enhanced immensely. The pattern of μ -CoV MPs is in good accord with the typical $\text{Co}_3\text{V}_2\text{O}_8$ pattern for the orthorhombic crystal (JCPDS no. 00-016-0675) phase with extremely good crystallinity [40,54–56]. The typical diffraction patterns (022), (220), (331), (400), (004), (511), and (440) are correspondingly centered at $2\theta = 27.5^{\circ}$, 29.3° , 34.6° , 42.8° , 53.4° , 58.7° and 63.1° . Table 2 provides a summary of the XRD results. Figure 3b is adapted from the work of Laverock et al. [57] and Sauerbrei et al. [58], who depicted that $\text{Co}_3\text{V}_2\text{O}_8$ orthovanadate ($[\text{VO}_4]^{3-}$) exists as discrete units in the crystal structure. $\text{Co}_3\text{V}_2\text{O}_8$ is typically crystallized in the centered orthorhombic space group $Cmca$, consisting of edge-sharing $-\text{Co}^{2+}\text{O}_6$ octahedra and $-\text{V}^{5+}\text{O}_4$ tetrahedra. Two inequivalent cobalt metal (M) sites exist within the crystal structure, referred to as M1, which is a cross-tie orientation over two sites per unit cell, and M2, which is a spine orientation over four sites per unit cell sites [57]. Compara-

tively, their metavanadate in CoV_2O_6 has a polymeric structure comprising $[\text{VO}_3]^-$ chains. These chains are established around the Co atom via VO_4 tetrahedra (corner-shared), VO_6 octahedra (corner-shared), and edge-shared VO_6 octahedra [54].

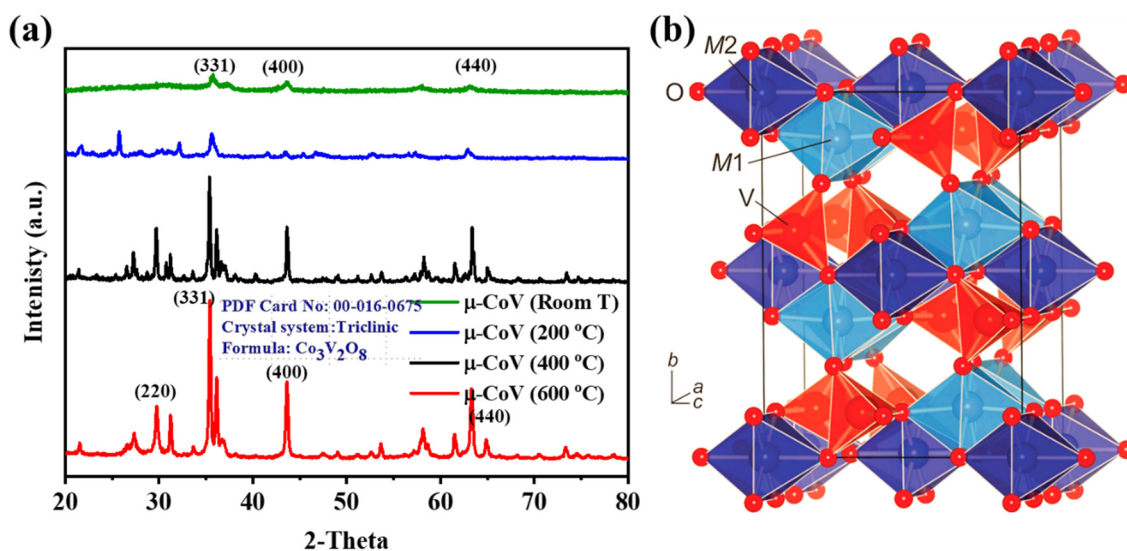


Figure 3. (a) Indexed XRD Pattern of $\mu\text{-CoV}$ MPs. (b) Crystal structure of $\mu\text{-CoV}$ MPs, containing MO_6 octahedra and VO_4 tetrahedra. Light blue M1 (cross tie) and dark blue M2 (spine) are two distinct inequivalent regions. M1 and M2 represent cobalt metal in our case. Reprinted with permission from Ref. [57]. 2013 Phys. Rev. B.

Table 2. XRD Characteristics of as-synthesized $\mu\text{-CoV}$ MPs.

Metal Vanadate (Code)	XRD Entry # (Phase Type)	Formula Unit	Ref.
Cobalt vanadate ($\mu\text{-CoV}$ MPs)	00-016-0675 (orthorhombic)	$\text{Co}_3(\text{VO}_4)_2$	[40,55,56]

To investigate the surface area and pore size distribution of $\mu\text{-CoV}$ MPs, we performed the BET analysis using N_2 adsorption/desorption isotherms. We obtained typical type IV isotherms with a hysteresis loop that attributed to the mesoporous nature of $\mu\text{-CoV}$ MPs, and the results are summarized in Table 3. The surface area of $131.22 \text{ m}^2 \text{ g}^{-1}$ is considered suitable for the adsorption of catalyzing species during the electrochemical analysis. It is important to mention here that the surface of the BET area of $\mu\text{-CoV}$ MPs component materials, i.e., Co_3O_4 and V_2O_5 is reported to be $52.9 \text{ m}^2 \text{ g}^{-1}$ and $1.9 \text{ m}^2 \text{ g}^{-1}$, respectively, by Xing and co-worker [39]. These are significantly lower values compared to the surface area of $\mu\text{-CoV}$ MPs, which is synthesized in a single step. Moreover, the pore size distribution $\mu\text{-CoV}$ MPs is recorded to be 5.8 nm, which lies within the mesoscale of 3 to 7 nm. The BET results confirmed the mesoporosity of $\mu\text{-CoV}$ MPs.

Table 3. Surface area and pore size distribution of $\mu\text{-CoV}$ MPs derived from the BET analysis.

Sample	Specific Surface Area	Pore Size (BJH)	Pore Volume (BJH)
$\mu\text{-CoV}$ MPs	$131.22 \text{ m}^2 \text{ g}^{-1}$	5.8 nm	0.18 nm

2.4. Electrochemical Oxygen Evolution (OER) Performance

The OER activity of the $\mu\text{-CoV}$ MPs deposited carbon paper electrode was measured in as-prepared SW electrolyte containing a 3-electrode electrochemical cell. The initial OER test was carried out to show the effect of catalyst dose on the OER performance of $\mu\text{-CoV}$ MPs. For this purpose, we have chosen five different concentrations of depositing materials,

i.e., 10, 20, 30, 40, and 50 μL , and loaded them separately over a carbon paper ($2 \times 1 \text{ cm}^2$) working electrode. The linear sweep voltammetry ($I-V$) at a scan rate of 5 mV s^{-1} was carried out to measure the OER activity of the catalysts of fabricated electrodes. As can be seen in Figure 4a, the direct dependence of OER on the current density is visible until 40 μL . The OER onset potential (V_{OER}) is shifted distinctly to cathodic value until 30 μL ; however, for 40 and 50 μL concentrations, the V_{OER} values are almost at a similar level. This can be ascribed to the fact that the optimum catalyst dose quantity acquired at 50 μL and the increased concentration of the catalyst or thickness of the fabricated layer would only impact the OER negligibly. Moreover, excess catalyst concentration can impact the OER performance negatively due to mass transport issues of the catalyst materials as widely reported in the literature [39,59–61]. Therefore, we have chosen 50 μL as an optimum catalyst amount for further OER measurements.

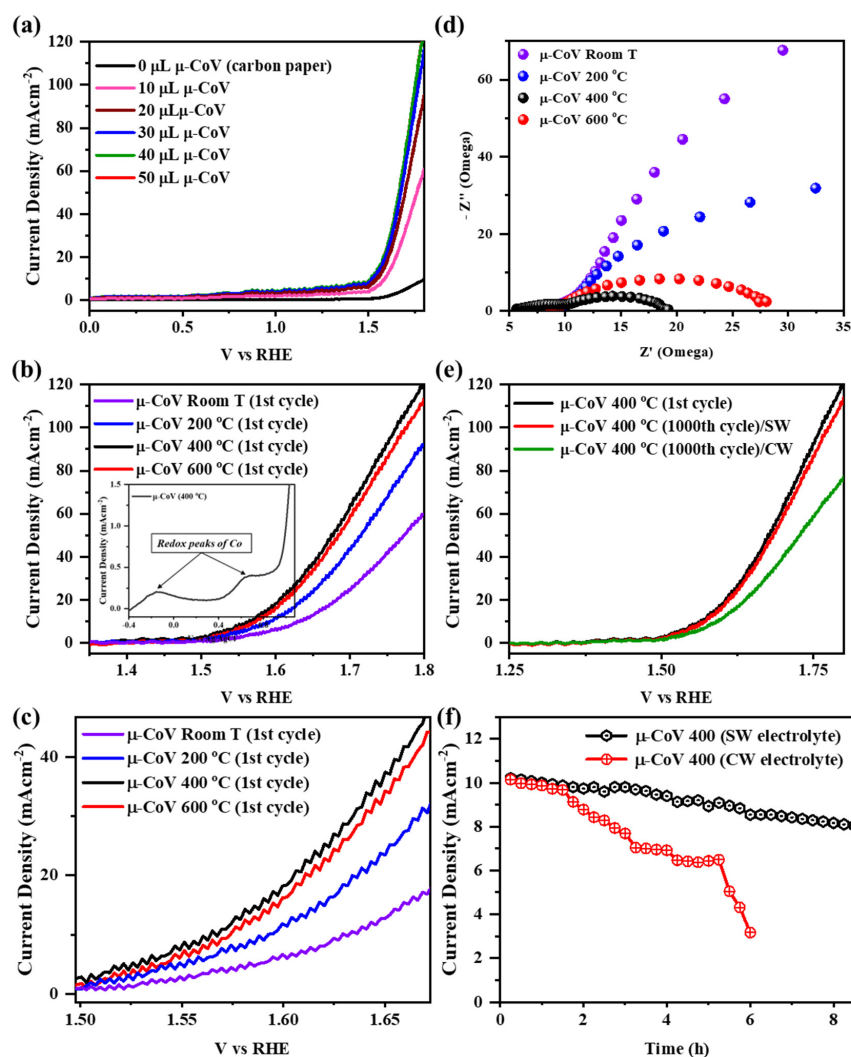


Figure 4. The OER activity analyses: (a) $\mu\text{-CoV}$ MPs mass loading effect on the OER polarization in SW; sweep rate: 5 mV s^{-1} . (b) $\mu\text{-CoV}$ MPs calcination temperature effect on the OER polarization in SW; sweep rate: 5 mV s^{-1} (Inset: Redox peaks indication of Co oxidation states). (c) Magnified region of Figure 4b from 1.50 to 1.70 V to realize the V_{onset} anodic shift. (d) Corresponding Nyquist plots of various calcined $\mu\text{-CoV}$ MPs electrodes in SW electrolyte recorded at $V_{\text{onset}}@10 \text{ mA}$ for each electrode by keeping the frequency range from 0.1 Hz to 100,000 Hz. (e) Comparative LSVs were acquired from $\mu\text{-CoV}$ MPs@400 $^{\circ}\text{C}$ electrodes in SW and CW to realize the electrochemical and mechanical stability in both media. (f) Comparative $I-t$ long-term stability curves of $\mu\text{-CoV}$ MPs@400 $^{\circ}\text{C}$ electrodes in SW and CW to realize the electrochemical and mechanical stability in both media. The initial LSV curves of $\mu\text{-CoV}$ MPs@400 $^{\circ}\text{C}$ electrodes in SW and CW yielded the same values.

Figure 4b,c depicts the temperature effect on the OER activity of the 50 μL $\mu\text{-CoV}$ MPs deposited over carbon paper. The OER activity seems to be dependent upon the calcination temperature. The as-synthesized samples showed a larger onset potential (V_{onset}) of 1.632 V to acquire 10 mA cm^{-2} current density. However, as indicated by the comparative LSV curves in Figure 4c, the $\mu\text{-CoV}$ MPs samples calcined at 200, 400, and 600 $^{\circ}\text{C}$ showed V_{onset} at 1.594, 1.559, and 1.574 V_{RHE} , respectively, to acquire 10 mA cm^{-2} current density. These values correspond to overpotentials 364, 329, and 344 mV, respectively, for the calcined samples. The best performance of $\mu\text{-CoV}$ MPs@400 $^{\circ}\text{C}$ anode can be attributed to the high surface area of the formed MPs. Though the crystallinity is not much improved compared to $\mu\text{-CoV}$ MPs@600 $^{\circ}\text{C}$, it is widely reported that with more crystallinity the particle size decreases, which could lead to a reduction in the V_{onset} values [39,53,62]. The good conductivity of the $\mu\text{-CoV}$ MPs@400 $^{\circ}\text{C}$ is also supported by electronic impedance spectroscopy (EIS). EIS generates semicircle Nyquist plots corresponding to the resistance offered by each sample. As revealed in Figure 4d, the radius of the $\mu\text{-CoV}$ MPs@400 $^{\circ}\text{C}$ Nyquist plot is less than $\mu\text{-CoV}$ MPs@600 $^{\circ}\text{C}$, which clearly indicates low resistivity and improved charge transfer behavior of $\mu\text{-CoV}$ MPs@400 $^{\circ}\text{C}$ anode. On the other hand, $\mu\text{-CoV}$ MPs@RT and $\mu\text{-CoV}$ MPs@200 $^{\circ}\text{C}$ anodes produced large radii Nyquist plots and therefore inhibit the charge transfer, comparatively. The EIS outcomes are in line with the electrical polarizabilities acquired from $\mu\text{-CoV}$ MPs@RT, $\mu\text{-CoV}$ MPs@200 $^{\circ}\text{C}$, $\mu\text{-CoV}$ MPs@400 $^{\circ}\text{C}$, and $\mu\text{-CoV}$ MPs@600 $^{\circ}\text{C}$ anodes.

Furthermore, we have investigated the electrochemical OER durability of the most stable $\mu\text{-CoV}$ MPs@400 $^{\circ}\text{C}$ electrodes in both SW and CW electrolytes in terms of LSV (I - V) polarization and chronoamperometric (I - t) analysis. Figure 4e provides a comparative assessment of the chemical durability of $\mu\text{-CoV}$ MPs@400 $^{\circ}\text{C}$ anodes within SW and CW electrolytes after 1000 LSV cycles. The $\mu\text{-CoV}$ MPs@400 $^{\circ}\text{C}$ in SW sustained its chemical stability after these cycles as the V_{onset} negligibly shifted anodically from 1.557 to 1.564 V_{RHE} . However, $\mu\text{-CoV}$ MPs@400 $^{\circ}\text{C}$ in CW could not sustain the intense electrolytic environment and shifted anodically from 1.557 to 1.596 V_{RHE} @ 10 mA cm^{-2} . The anodic shift in the case of $\mu\text{-CoV}$ MPs@400 $^{\circ}\text{C}$ in CW became more visible at higher potentials. To further support the SW and CW impact hypothesis, the long-term current-time (I - t) tests were accomplished by keeping the potential values constant at the corresponding value of 10 mA cm^{-2} in each case (Figure 4f). In the case of the $\mu\text{-CoV}$ MPs@400 $^{\circ}\text{C}$ electrode in SW, significant changes did not occur in the OER activity as the current density slightly declined for the first 3 h and 15 min. However, a slight chemical shift in behavior was observed, leading to a current decline at a slow rate. This can be attributed to the loss of electrolytic activity in the highly concentrated electrolytic environment. However, the electrode sustained a pronounced chemical and mechanical state and maintained >80% OER current density for a brief time of 8 h. On the contrary, as expected the $\mu\text{-CoV}$ MPs@400 $^{\circ}\text{C}$ electrode in CW experienced substantial electrochemical corrosion after 2 h. The $\mu\text{-CoV}$ MPs@400 $^{\circ}\text{C}$ electrode in CW could not sustain the OER activity after this period and completely deteriorated after 6 h. Visually the loaded electrode material particles were separated from the electrode and suspended in the electrolytic solution. Having extremely high concentrations of active salts, the CW is assumed to cause more chemical and mechanical corrosion to the electrode surface than the SW. Table 4 provides a literature comparison of various cobalt vanadate-based electrode materials for OER, including their morphology, synthesis method, electrolyte, V_{OER} @ 10 mA , and time-dependent electrochemical stability. Briefly, Co_2O_8 NPs synthesized through stirring-assisted wet chemistry synthesis showed stable performance for 3 h [39]. In a similar study, $\text{Co}_3\text{V}_2\text{O}_8$ nanosheets synthesized through DMF, ethanol and glycol solvent-derived synthesis have demonstrated 23% activity loss after only 150 CV cycles [63]. Co-V mixed oxide catalysts (CoVO_x) synthesized through aerosol-assisted chemical vapor deposition showed stable performance for 6 h [64], while Co and V mixed at 1:1 synthesized through chemical mixing and high-temperature annealing showed stable performance for 18 h [65]. Most of these studies performed OER in KOH electrolytes. Comparatively, the as-synthesized $\mu\text{-CoV}$ MPs@400 $^{\circ}\text{C}$ electrodes

in SW in the current study are highly competitive in terms of electrochemical long-term ($I-t$) stability and overpotential with the same class of materials. The mechanism of OER over μ -CoV MPs@400 °C follows the same pattern as most cobalt-based materials [66–69]. In both SW and CW electrolytes, the rate of OER proceeded with almost similar kinetics, initially. However, as time passed, the CW electrolyte posed substantial mechanical and chemical challenges to the μ -CoV MPs@400 °C electrode. In response, the rate of reaction was slightly reduced from 199 mV dec⁻¹ to 206 mV dec⁻¹, as shown by the high Tafel slope value in Figure S2 (obtained from μ -CoV MPs@400 °C in CW electrolyte after 1 h OER). The substrate's surface showed much deterioration after 90 min; therefore, the Tafel values were not measured afterwards. Based on the literature, it is assumed that the μ -CoV MP established an interaction with $-OH$ ions as follows [54,70].

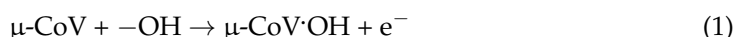


Table 4. The OER activity comparison of μ -CoV MPs with the same class of reported materials.

Electrode Material [Ref.]	Morphology and Particles Size	Synthesis Method	Electrolyte	$V_{OER}@10\text{ mA}$	Stability
$\text{Co}_3\text{V}_2\text{O}_8$ MPs (This work)	globular shaped particles of 3–5 μm size	Pluronic-123 assisted solvothermal synthesis	Seawater	1.557	Sustained >80% OER stability after 8 h, while activity lost <1% after 1000 LSV cycles.
$\text{Co}_3\text{V}_2\text{O}_8$ MPs (This work)	globular shaped particles of 3–5 μm size	Pluronic-123 assisted solvothermal synthesis	Connate water	1.557	Not sustained OER activity after 2 h, while activity lost >10% after 1000 LSV cycles.
$\text{Co}_3\text{V}_2\text{O}_8$ NPs [39]	Irregular nanoparticles of average size 20 nm	Stirring-assisted Wet chemistry synthesis	1 M KOH	1.595	Stable for 3 h
$\text{Co}_3\text{V}_2\text{O}_8$ nanosheets [63]	Ultrafine 2D-nanosheets at the nanoscale level	DMF, ethanol and glycol solvent-derived synthesis	1 M KOH	1.563	Optimized catalyst lost 23% activity after 150 CV cycles
$\text{Co}_3\text{V}_2\text{O}_8$ nanosheets [54]	Irregular spheres with diameters ranging from 40 to 250 nm	Sol-gel method followed by calcination	1 M KOH	1.74	The stability results for $\text{Co}_3\text{V}_2\text{O}_8$ are not provided.
Co–V mixed oxide catalysts (CoVO _x) [64]	A network of interwoven nanofibers appeared at the nanoscale level	Aerosol assisted chemical vapor deposition synthesis	0.5 M KOH	1.54@20 mA	Stable for 6 h, while <1% activity loss after 500 cycles.
Co and V mixed at 1:1 [65]	Nanoclusters formed by large agglomeration	Chemical mixing and high-temperature annealing	1 M KOH	0.43 vs. Ag/AgCl	Stable for 18 h

This step is also regarded as a rate-determining step due to its sluggishness, which is followed by the oxygen evolution step. Furthermore, the EIS analysis in Figure 4d also revealed that the annealing temperature controlled the physicochemical processes responsible for the activity enhancement. The appearance of two distinct semicircles in the Nyquist plot demonstrated the effect of the charge transfer resistance (R_{ct}) with double-layer capacitance (C_{dl}) and the effect of the adsorption resistance (R_a) with the adsorption capacitance (C_a) [71]. The obtained lower R_{ct} value of μ -CoV MPs@400 °C electrode in SW

allows a higher voltage to be available for adsorption capacitance that can be attributed to the microstructures and high surface area.

The SEM images in Figure 5 are acquired from the substrate after the OER activity in SW and CW. Figure 5a,b indicates that after 8 h OER stability in SW, the morphology of μ -CoV MPs squeezed to plate-shaped particles with distinct boundaries from the original bulged globular shape particles. It is expected that due to this effect, the porosity and surface area of electrode materials were impacted negatively, which led to a decrease in the OER activity over time. The possible reason for this plating can be attributed to the electrochemical etching and corrosion of the interfacial particles within the SW electrolyte [72–74].

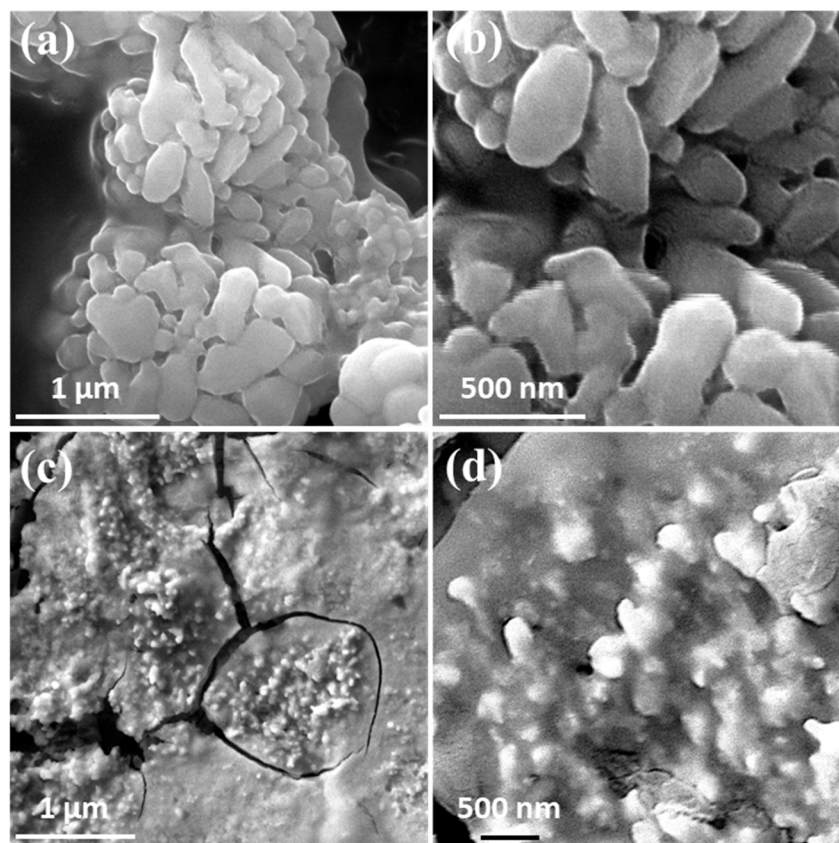


Figure 5. Low and high-resolution FESEM of μ -CoV MPs after OER activity in (a,b) SW electrolyte and (c,d) CW electrolyte.

In comparison, the CW electrolyte caused stronger etching due to the high concentration of salts, which almost destroyed the original morphology of μ -CoV MPs and also caused cracks within the substrate film at the micro level (Figure 5 c,d taken after the OER stability test). This caused a sharp current density decline in OER after a short period compared to SW electrolytes. Similarly, the XRD results in Figure S1 also confirmed that in the case of 8 h OER activity within SW, the crystallinity was reduced immensely compared to the original substrate.

After all these analyses, it can be stated that CW is unsuitable for the OER activity of μ -CoV MPs due to the extremely harsh ion effect caused by high concentrations of brines. However, the stability performance of μ -CoV MPs in SW is reasonable and is expected to further improve by properly modifying the parent material, applying a passive layer, or adding a suitable cocatalyst to control the electrochemical kinetics [18,75]. This study can enthruse researchers to scrupulously undertake post-catalytic electrochemical and analytical characterizations for an in-depth understanding of the various mechanisms involved during the OER activity of μ -CoV MPs electrodes within high-concentration and naturally available brine electrolytes.

3. Experimental Section

3.1. Materials

NH_4VO_3 (Sigma Aldrich, St. Louis, MO, USA) as a vanadate source, hydrated cobalt nitrate salt precursors, i.e., $\text{Co}(\text{NO}_3)_2 \cdot 6\text{H}_2\text{O}$ (Sigma Aldrich), Pluronic polymer [triblock copolymer, i.e., PEO-PPO-PEO (*P-123*)] as a surfactant source (Sigma Aldrich). Absolute ethanol and pure deionized (DI) water with a conductivity of $0.05501 \mu\text{S}/\text{cm}$ and resistivity of $18.18 \text{ M}\Omega \cdot \text{cm}$ at 25°C were used for reaction and washing purposes. All the salts for preparing seawater and connate (or formation) water were obtained from Sigma Aldrich with maximum purity. SW and CW compositions were prepared according to Table 5 [76,77]. All the fluids were filtered to remove the undissolved moieties before use in the respective experiments.

Table 5. Composition of seawater and connate (formation) water.

Component Salts	Connate Water (g/L)	Seawater (g/L)
NaHCO_3	0.487	0.165
Na_2SO_4	0.518	6.339
NaCl	150.446	41.17
$\text{CaCl}_2 \cdot 2\text{H}_2\text{O}$	69.841	2.387
$\text{MgCl}_2 \cdot 6\text{H}_2\text{O}$	20.396	17.416
Total	241.688	67.480

3.2. Characterization

The phase structure and crystallinity characterization of the metal vanadates were analyzed using a Cu $K\alpha$ $\lambda = 0.15406 \text{ nm}$ radiation from a high-resolution X-ray diffractometer (XRD, Rigaku MiniFlex, Rigaku Corp., Tokyo, Japan). The sample was scanned from $2\theta = 10^\circ$ to 80° at a scan rate of 0.05 degrees/min, while the morphological characterizations were obtained on a field emission scanning electron microscope (LYRA 3 Dual Beam instrument) operated at an acceleration voltage of 20 kV (Tescan, Brno, Czech Republic). Pore size distributions and surface area were calculated by Brunauer-Emmett-Teller (BET) formulations using data from volumetric nitrogen adsorption/desorption experiments (Micromeritics ASAP 2020, Micromeritics, Norcross, GA, USA). Pore size distribution was estimated by applying the Barrett-Joyner-Halenda (BJH) method to the desorption branch of the isotherm.

3.3. Electrochemical Measurements

A three-electrode cell controlled by Gamry 600+ potentiostat (Gamry Instruments, Philadelphia, PA, USA) was established to measure the OER activity of the $\mu\text{-CoV}$ deposited working electrode (carbon paper, $2 \times 1 \text{ cm}^2$). A $2 \times 1 \text{ cm}^2$ Pt gauze worked as a counter electrode, while Ag/AgCl acted as a reference. All the potentials were standardized against a reversible hydrogen electrode (RHE) using the Nernst equation ($E_{\text{RHE}} = E_{\text{Ag}/\text{AgCl}} + 0.0591 \text{ pH} + E_{0\text{Ag}/\text{AgCl}}$) [78]. The fabrication of the working electrode was performed by adding 5 mg $\mu\text{-CoV}$ MPs powder dispersed in 1 mL $0.0625 \text{ Nafion}/0.7325 \text{ water}/0.20 \text{ ethanol}$ mass rate by sonication for 3 min to produce a highly dispersed ink. Then, $10, 20, 30, 40,$ and $50 \mu\text{L}$ of the dispersion were loaded onto a carbon paper ($2 \times 1 \text{ cm}^2$) working electrode separately to obtain the optimized catalyst dose. The linear sweep voltammetry (I - V) at a scan rate of 5 mV s^{-1} and amperometry (I - t) tools (for time-dependent stability test at 10 mA cm^{-2}) were used to measure the OER activity of the loaded catalysts. The electrochemical impedance spectra (EIS) were recorded to establish electrode kinetics at V_{RHE} equivalent to 10 mA cm^{-2} in SW.

4. Conclusions

For the first time, the binary metal oxide of μ -CoV MPs was investigated in SW and CW for durable electrochemical OER activity. The *P-123* was used to obtain the μ -CoV microstructure morphology with embedded seeds structure in a single step. The *P-123*-assisted μ -CoV MPs were subjected to annealing at various temperatures and the OER activity indicated that the μ -CoV MPs@400 °C is the best electrocatalysts in terms of onset potential value and electrochemical durability in SW. The μ -CoV MPs@400 °C in SW sustained its chemical stability after 1000 cycles as the V_{onset} marginally shifted anodically from 1.557 to 1.564 V_{RHE} . The time-dependent stability test indicated that the μ -CoV MPs@400 °C electrode sustained a pronounced >80% OER current density for a period of 8 h. On the contrary, as expected, the μ -CoV MPs@400 °C electrode in CW experienced substantial electrochemical corrosion after 2 h. Having extremely high concentrations of active salts, the CW is assumed to cause more chemical and mechanical corrosion and etching to the electrode surface than the SW. These analyses concluded that further modifications and optimization of μ -CoV MPs materials can be suitably applied in commercially available SW electrolytes for enhanced OER applications to universally boost the hydrogen economy.

Supplementary Materials: The following supporting information can be downloaded at: <https://www.mdpi.com/article/10.3390/catal13030636/s1>. Figure S1: XRD patterns of μ -CoV MPs-400 °C before OER and after OER in SW, Figure S2: Tafel plots under different electrolytic conditions.

Funding: This research work is supported by the Brain Pool program funded by the Ministry of Science and ICT through the National Research Foundation of Korea (grant number NRF-2021H1D3A2A02044205).

Acknowledgments: The author acknowledges the support of WISE-LAB, Chung Ang University, South Korea for providing the all required support.

Conflicts of Interest: The authors declare no conflict of interest.

References

1. Liu, X.; Zhao, C.; Muhmood, T.; Yang, X. Regulating the Assembly of Precursors of Carbon Nitrides to Improve Photocatalytic Hydrogen Production. *Catalysts* **2022**, *12*, 1634. [CrossRef]
2. Butt, F.K.; Tahir, M.; Cao, C.; Idrees, F.; Ahmed, R.; Khan, W.S.; Ali, Z.; Mahmood, N.; Tanveer, M.; Mahmood, A.; et al. Synthesis of Novel ZnV_2O_4 Hierarchical Nanospheres and Their Applications as Electrochemical Supercapacitor and Hydrogen Storage Material. *ACS Appl. Mater. Interfaces* **2014**, *6*, 13635–13641. [CrossRef] [PubMed]
3. Wang, E.; Mahmood, A.; Chen, S.G.; Sun, W.; Muhmood, T.; Yang, X.; Chen, Z. Solar-Driven Photocatalytic Reforming of Lignocellulose into H_2 and Value-Added Biochemicals. *ACS Catal.* **2022**, *12*, 11206–11215. [CrossRef]
4. Mahmood, A.; Muhmood, T.; Ahmad, F. Carbon nanotubes heterojunction with graphene like carbon nitride for the enhancement of electrochemical and photocatalytic activity. *Mater. Chem. Phys.* **2022**, *278*, 125640. [CrossRef]
5. Tayebi, M.; Lee, B.-K. Recent advances in BiVO_4 semiconductor materials for hydrogen production using photoelectrochemical water splitting. *Renew. Sustain. Energy Rev.* **2019**, *111*, 332–343. [CrossRef]
6. Khan, I.; Qurashi, A. Shape Controlled Synthesis of Copper Vanadate Platelet Nanostructures, Their Optical Band Edges, and Solar-Driven Water Splitting Properties. *Sci. Rep.* **2017**, *7*, 14370. [CrossRef]
7. Khan, I.; Jalilov, A.; Fujii, K.; Qurashi, A. Quasi-1D Aligned Nanostructures for Solar-Driven Water Splitting Applications: Challenges, Promises, and Perspectives. *Sol. RRL* **2021**, *5*, 2000741. [CrossRef]
8. Song, J.; Wei, C.; Huang, Z.F.; Liu, C.; Zeng, L.; Wang, X.; Xu, Z.J. A review on fundamentals for designing oxygen evolution electrocatalysts. *Chem. Soc. Rev.* **2020**, *49*, 2196–2214. [CrossRef]
9. Exner, K.S.; Over, H. Beyond the Rate-Determining Step in the Oxygen Evolution Reaction over a Single-Crystalline $\text{IrO}_2(110)$ Model Electrode: Kinetic Scaling Relations. *ACS Catal.* **2019**, *9*, 6755–6765. [CrossRef]
10. Cherevko, S.; Zeradjanin, A.R.; Keeley, G.P.; Mayrhofer, K.J.J. A Comparative Study on Gold and Platinum Dissolution in Acidic and Alkaline Media. *J. Electrochem. Soc.* **2014**, *161*, H822–H830. [CrossRef]
11. Khan, I.; Lee, J.H.; Park, J.; Wooh, S. Nano/micro-structural engineering of Nafion membranes for advanced electrochemical applications. *J. Saudi Chem. Soc.* **2022**, *26*, 101511. [CrossRef]
12. Lutterman, D.A.; Surendranath, Y.; Nocera, D.G. A Self-Healing Oxygen-Evolving Catalyst. *J. Am. Chem. Soc.* **2009**, *131*, 3838–3839. [CrossRef] [PubMed]
13. Reddy, N.K.; Winkler, S.; Koch, N.; Pinna, N. Electrochemical water oxidation of ultrathin cobalt oxide-based catalyst supported onto aligned ZnO nanorods. *ACS Appl. Mater. Interfaces* **2016**, *8*, 3226–3232. [CrossRef] [PubMed]

14. Kanan, M.W.; Nocera, D.G. In Situ Formation of an Oxygen-Evolving Catalyst in Neutral Water Containing Phosphate and Co^{2+} . *Science (80-)* **2008**, *321*, 1072–1075. [[CrossRef](#)]
15. Mansha, M.; Khan, I.; Ullah, N.; Qurashi, A.; Sohail, M. Visible-light driven photocatalytic oxygen evolution reaction from new poly(phenylene cyanovinylenes). *Dye. Pigment.* **2017**, *143*, 95–102. [[CrossRef](#)]
16. Fan, R.Y.; Xie, J.Y.; Yu, N.; Chai, Y.M.; Dong, B. Interface design and composition regulation of cobalt-based electrocatalysts for oxygen evolution reaction. *Int. J. Hydrogen Energy* **2022**, *47*, 10547–10572. [[CrossRef](#)]
17. Zhang, Q.; Duan, Z.; Li, M.; Guan, J. Atomic cobalt catalysts for the oxygen evolution reaction. *Chem. Commun.* **2020**, *56*, 794–797. [[CrossRef](#)]
18. Moysiadou, A.; Lee, S.; Hsu, C.S.; Chen, H.M.; Hu, X. Mechanism of Oxygen Evolution Catalyzed by Cobalt Oxyhydroxide: Cobalt Superoxide Species as a Key Intermediate and Dioxygen Release as a Rate-Determining Step. *J. Am. Chem. Soc.* **2020**, *142*, 11901–11914. [[CrossRef](#)]
19. Haase, F.T.; Bergmann, A.; Jones, T.E.; Timoshenko, J.; Herzog, A.; Jeon, H.S.; Rettenmaier, C.; Cuenya, B.R. Size effects and active state formation of cobalt oxide nanoparticles during the oxygen evolution reaction. *Nat. Energy* **2022**, *7*, 765–773. [[CrossRef](#)]
20. Bhattacharyya, K.; Auer, A.A. Oxygen Evolution Reaction Electrocatalysis on Cobalt(oxy)hydroxide: Role of Fe Impurities. *J. Phys. Chem. C* **2022**, *126*, 18623–18635. [[CrossRef](#)]
21. Liu, Y.; Ran, N.; Ge, R.; Liu, J.; Li, W.; Chen, Y.; Feng, L.; Che, R. Porous Mn-doped cobalt phosphide nanosheets as highly active electrocatalysts for oxygen evolution reaction. *Chem. Eng. J.* **2021**, *425*, 131642. [[CrossRef](#)]
22. Yan, L.; Zhang, B.; Liu, Z.; Zhu, J. Synergy of copper doping and oxygen vacancies in porous CoOOH nanoplates for efficient water oxidation. *Chem. Eng. J.* **2021**, *405*, 126198. [[CrossRef](#)]
23. Niu, W.; Shi, J.; Ju, L.; Li, Z.; Orlovskaya, N.; Liu, Y.; Yang, Y. Understanding Synergism of Cobalt Metal and Copper Oxide toward Highly Efficient Electrocatalytic Oxygen Evolution. *ACS Catal.* **2018**, *8*, 12030–12040. [[CrossRef](#)]
24. Zhao, J.; He, Y.; Wang, J.; Zhang, J.; Qiu, L.; Chen, Y.; Zhong, C.; Han, X.; Deng, Y.; Hu, W. Regulating metal active sites of atomically-thin nickel-doped spinel cobalt oxide toward enhanced oxygen electrocatalysis. *Chem. Eng. J.* **2022**, *435*, 134261. [[CrossRef](#)]
25. Liu, S.; Zhang, B.; Cao, Y.; Wang, H.; Zhang, Y.; Zhang, S.; Li, Y.; Gong, H.; Liu, S.; Yang, Z.; et al. Understanding the Effect of Nickel Doping in Cobalt Spinel Oxides on Regulating Spin State to Promote the Performance of the Oxygen Reduction Reaction and Zinc-Air Batteries. *ACS Energy Lett.* **2022**, *8*, 159–168. [[CrossRef](#)]
26. Ashraf, M.; Khan, I.; Baig, N.; Hendi, A.H.; Ehsan, M.F.; Sarfraz, N. A Bifunctional 2D Interlayered $\beta\text{-Cu}_2\text{V}_2\text{O}_7/\text{Zn}_2\text{V}_2\text{O}_6$ (CZVO) Heterojunction for Solar-Driven Nonsacrificial Dye Degradation and Water Oxidation. *Energy Technol.* **2021**, *9*, 2100034. [[CrossRef](#)]
27. Khan, A.Z.; Khan, I.; Sufyan, A.; Anjum, D.; Qurashi, A. Activation of $\text{Ni}_2\text{V}_2\text{O}_7$ to nonstoichiometric NiV_3O_8 for solar-driven photoelectrochemical water oxidation. *J. Environ. Chem. Eng.* **2021**, *9*, 105526. [[CrossRef](#)]
28. Khan, I.; Khan, A.A.Z.; Sufyan, A.; Khan, M.Y.; Inayath Basha, S.; Khan, A.A.Z. Ultrasonically controlled growth of monodispersed octahedral BiVO_4 microcrystals for improved photoelectrochemical water oxidation. *Ultrason. Sonochem.* **2020**, *68*, 105233. [[CrossRef](#)] [[PubMed](#)]
29. Khan, I.; Ali, S.; Mansha, M.; Qurashi, A. Sonochemical assisted hydrothermal synthesis of pseudo-flower shaped Bismuth vanadate (BiVO_4) and their solar-driven water splitting application. *Ultrason. Sonochem.* **2017**, *36*, 386–392. [[CrossRef](#)] [[PubMed](#)]
30. Seki, T.; Okuzono, T.; Toyotama, A.; Yamanaka, J. Mechanism of diffusiophoresis with chemical reaction on a colloidal particle. *Phys. Rev. E* **2019**, *99*, 012608. [[CrossRef](#)]
31. Keh, H.J. Diffusiophoresis. In *Encyclopedia of Microfluidics and Nanofluidics*; Springer: Boston, MA, USA, 2008; pp. 365–369.
32. Velegol, D.; Garg, A.; Guha, R.; Kar, A.; Kumar, M. Origins of concentration gradients for diffusiophoresis. *Soft Matter* **2016**, *12*, 4686–4703. [[CrossRef](#)]
33. Dresp, S.; Dionigi, F.; Klingenhof, M.; Strasser, P. Direct electrolytic splitting of seawater: Opportunities and challenges. *ACS Energy Lett.* **2019**, *4*, 933–942. [[CrossRef](#)]
34. Dresp, S.; Ngo Thanh, T.; Klingenhof, M.; Brückner, S.; Hauke, P.; Strasser, P. Efficient direct seawater electrolyzers using selective alkaline NiFe-LDH as OER catalyst in asymmetric electrolyte feeds. *Energy Environ. Sci.* **2020**, *13*, 1725–1729. [[CrossRef](#)]
35. Yu, L.; Xiao, J.; Huang, C.; Zhou, J.; Qiu, M.; Yu, Y.; Ren, Z.; Chu, C.-W.; Yu, J.C. High-performance seawater oxidation by a homogeneous multimetallic layered double hydroxide electrocatalyst. *Proc. Natl. Acad. Sci. USA* **2023**, *119*, e2202382119. [[CrossRef](#)] [[PubMed](#)]
36. Yu, L.; Zhu, Q.; Song, S.; McElhenny, B.; Wang, D.; Wu, C.; Qin, Z.; Bao, J.; Yu, Y.; Chen, S.; et al. Non-noble metal-nitride based electrocatalysts for high-performance alkaline seawater electrolysis. *Nat. Commun.* **2019**, *10*, 5106. [[CrossRef](#)] [[PubMed](#)]
37. Liu, W.; Li, J.; Li, W.; Xu, H.; Zhang, C.; Qiu, X. Inhibition of transition metals dissolution in cobalt-free cathode with ultrathin robust interphase in concentrated electrolyte. *Nat. Commun.* **2020**, *11*, 3629. [[CrossRef](#)] [[PubMed](#)]
38. Yang, L.; Zhou, L.; Wang, M.; Qi, Y.; Guo, D.; Li, H.; Chen, X.; Wang, S. Transition Metal-Based Electrocatalysts for Seawater Oxidation. *Adv. Mater. Interfaces* **2022**, *9*, 2201486. [[CrossRef](#)]
39. Xing, M.; Kong, L.-B.; Liu, M.-C.; Liu, L.-Y.; Kang, L.; Luo, Y.-C. Cobalt vanadate as highly active, stable, noble metal-free oxygen evolution electrocatalyst. *J. Mater. Chem. A* **2014**, *2*, 18435–18443. [[CrossRef](#)]
40. Zhang, Y.; Liu, Y.; Chen, J.; Guo, Q.; Wang, T.; Pang, H. Cobalt vanadium oxide thin nanoplates: Primary electrochemical capacitor application. *Sci. Rep.* **2015**, *4*, 5687. [[CrossRef](#)]

41. Yu, Y.; Zhu, W.; Hua, L.; Yang, H.; Qiao, Y.; Zhang, R.; Guo, L.; Zhao, X.; Hou, Z. Ionic liquid-Pluronic P123 mixed micelle stabilized water-soluble Ni nanoparticles for catalytic hydrogenation. *J. Colloid Interface Sci.* **2014**, *415*, 117–126. [[CrossRef](#)]
42. Barick, K.C.; Ekta; Gawali, S.L.; Sarkar, A.; Kunwar, A.; Priyadarsini, K.I.; Hassan, P.A. Pluronic stabilized Fe₃O₄ magnetic nanoparticles for intracellular delivery of curcumin. *RSC Adv.* **2016**, *6*, 98674–98681. [[CrossRef](#)]
43. Khan, I.; Ibrahim, A.A.M.; Sohail, M.; Qurashi, A. Sonochemical assisted synthesis of RGO/ZnO nanowire arrays for photoelectrochemical water splitting. *Ultrason. Sonochem.* **2017**, *37*, 669–675. [[CrossRef](#)]
44. Saeed, K.; Khan, I. Preparation and properties of single-walled carbon nanotubes/poly(butylene terephthalate) nanocomposites. *Iran. Polym. J.* **2014**, *23*, 53–58. [[CrossRef](#)]
45. Mahbulbul, I.M.; Chong, T.H.; Khaleduzzaman, S.S.; Shahrul, I.M.; Saidur, R.; Long, B.D.; Amalina, M.A. Effect of Ultrasonication Duration on Colloidal Structure and Viscosity of Alumina–Water Nanofluid. *Ind. Eng. Chem. Res.* **2014**, *53*, 6677–6684. [[CrossRef](#)]
46. Sivakumar, M.; Pandit, A.B. Wastewater treatment: A novel energy efficient hydrodynamic cavitation technique. *Ultrason. Sonochem.* **2002**, *9*, 123–131. [[CrossRef](#)]
47. Sakai, T.; Kurosawa, H.; Okada, T.; Mishima, S. Vesicle formation in mixture of a PEO-PPO-PEO block copolymer (Pluronic P123) and a nonionic surfactant (Span 65) in water. *Colloids Surfaces A Physicochem. Eng. Asp.* **2011**, *389*, 82–89. [[CrossRef](#)]
48. García-Pérez, U.M.; Martínez-De La Cruz, A.; Sepúlveda-Guzmán, S.; Peral, J. Low-temperature synthesis of BiVO₄ powders by Pluronic-assisted hydrothermal method: Effect of the surfactant and temperature on the morphology and structural control. *Ceram. Int.* **2014**, *40*, 4631–4638. [[CrossRef](#)]
49. Park, G.C.; Seo, T.Y.; Park, C.H.; Lim, J.H.; Joo, J. Effects of Calcination Temperature on Morphology, Microstructure, and Photocatalytic Performance of TiO₂ Mesocrystals. *Ind. Eng. Chem. Res.* **2017**, *56*, 8235–8240. [[CrossRef](#)]
50. Rosca, I.D.; Watari, F.; Uo, M. Microparticle formation and its mechanism in single and double emulsion solvent evaporation. *J. Control. Release* **2004**, *99*, 271–280. [[CrossRef](#)]
51. Campbell, Z.S.; Baro, S.; Gao, Y.; Li, F.; Abolhasani, M. Flow Synthesis of Single and Mixed Metal Oxides. *Chem. Methods* **2022**, *2*, e202200007. [[CrossRef](#)]
52. Dowding, I.; Hassani, M.; Sun, Y.; Veysset, D.; Nelson, K.A.; Schuh, C.A. Particle size effects in metallic microparticle impact-bonding. *Acta Mater.* **2020**, *194*, 40–48. [[CrossRef](#)]
53. Suharyadi, E.; Pratiwi, S.H.; Indrayana, I.P.T.; Kato, T.; Iwata, S.; Ohto, K. Effects of annealing temperature on microstructural, magnetic properties, and specific absorption rate of Zn-Ni ferrite nanoparticles. *Mater. Res. Express* **2021**, *8*, 036101. [[CrossRef](#)]
54. Mondal, A.; Ganguli, S.; Inta, H.R.; Mahalingam, V. Influence of Vanadate Structure on Electrochemical Surface Reconstruction and OER Performance of CoV₂O₆ and Co₃V₂O₈. *ACS Appl. Energy Mater.* **2021**, *4*, 5381–5387. [[CrossRef](#)]
55. Ji, Y.; Ma, Y.; Liu, R.; Ma, Y.; Cao, K.; Kaiser, U.; Varzi, A.; Song, Y.-F.; Passerini, S.; Streb, C. Modular development of metal oxide/carbon composites for electrochemical energy conversion and storage. *J. Mater. Chem. A* **2019**, *7*, 13096–13102. [[CrossRef](#)]
56. Yang, J.; Wu, M.; Gong, F.; Feng, T.; Chen, C.; Liao, J. Facile and controllable synthesis of solid Co₃V₂O₈ micro-pencils as a highly efficient anode for Li-ion batteries. *RSC Adv.* **2017**, *7*, 24418–24424. [[CrossRef](#)]
57. Laverock, J.; Chen, B.; Preston, A.R.H.; Smith, K.E.; Wilson, N.R.; Balakrishnan, G.; Glans, P.-A.; Guo, J.-H. Electronic structure of the kagome staircase compounds Ni₃V₂O₈ and Co₃V₂O₈. *Phys. Rev. B* **2013**, *87*, 125133. [[CrossRef](#)]
58. Sauerbrei, E.E.; Faggiani, R.; Calvo, C. Refinement of the crystal structure of Co₃V₂O₈ and Ni₃V₂O₈. *Acta Crystallogr. Sect. B Struct. Crystallogr. Cryst. Chem.* **1973**, *29*, 2304–2306. [[CrossRef](#)]
59. Nagy, E.; Vitai, M. Analysis of Mass Transport through Anisotropic, Catalytic/Bio-Catalytic Membrane Reactors. *Catalysts* **2019**, *9*, 358. [[CrossRef](#)]
60. Alfath, M.; Lee, C.W. Recent Advances in the Catalyst Design and Mass Transport Control for the Electrochemical Reduction of Carbon Dioxide to Formate. *Catalysts* **2020**, *10*, 859. [[CrossRef](#)]
61. Yu, L.; Sun, S.; Li, H.; Xu, Z.J. Effects of catalyst mass loading on electrocatalytic activity: An example of oxygen evolution reaction. *Fundam. Res.* **2021**, *1*, 448–452. [[CrossRef](#)]
62. Pikula, T.; Szumiata, T.; Siedliska, K.; Mitsiuk, V.I.; Panek, R.; Kowalczyk, M.; Jartych, E. The Influence of Annealing Temperature on the Structure and Magnetic Properties of Nanocrystalline BiFeO₃ Prepared by Sol–Gel Method. *Metall. Mater. Trans. A Phys. Metall. Mater. Sci.* **2022**, *53*, 470–483. [[CrossRef](#)]
63. Hao, M.; Xiao, M.; Qian, L.; Miao, Y. Synthesis of cobalt vanadium nanomaterials for efficient electrocatalysis of oxygen evolution. *Front. Chem. Sci. Eng.* **2018**, *12*, 409–416. [[CrossRef](#)]
64. Ehsan, M.A.; Saeed, A.H.; Sharif, M.; Rehman, A. Direct deposition of amorphous cobalt-vanadium mixed oxide films for electrocatalytic water oxidation. *ACS Omega* **2019**, *4*, 12671–12679. [[CrossRef](#)]
65. Keerthana, S.; Yuvakkumar, R.; Ravi, G.; Pannipara, M.; Al-Sehemi, A.G.; Velauthapillai, D. Cobalt Vanadium Oxide Nanoclusters for Oxygen Evolution Reaction. *ECS J. Solid State Sci. Technol.* **2021**, *10*, 071003. [[CrossRef](#)]
66. Xiao, G.; Chen, W.; Cai, Y.; Zhang, S.; Wang, D.; Cai, D. Facile Synthesis of Sulfate-Intercalated CoFe LDH Nanosheets Derived from Two-Dimensional ZIF-9(III) for Promoted Oxygen Evolution Reaction. *Catalysts* **2022**, *12*, 688. [[CrossRef](#)]
67. Bai, X.; Duan, Z.; Nan, B.; Wang, L.; Tang, T.; Guan, J. Unveiling the active sites of ultrathin Co-Fe layered double hydroxides for the oxygen evolution reaction. *Chin. J. Catal.* **2022**, *43*, 2240–2248. [[CrossRef](#)]
68. Zhang, Q.; Guan, J. Applications of single-atom catalysts. *Nano Res.* **2021**, *15*, 38–70. [[CrossRef](#)]
69. Chen, D.; Pan, L.; Pei, P.; Song, X.; Ren, P.; Zhang, L. Cobalt-based oxygen electrocatalysts for zinc-air batteries: Recent progress, challenges, and perspectives. *Nano Res.* **2022**, *15*, 5038–5063. [[CrossRef](#)]

70. Gyanprakash, D.M.; Sharma, G.P.; Gupta, P.K. Isovalent anion-induced electrochemical activity of doped $\text{Co}_3\text{V}_2\text{O}_8$ for oxygen evolution reaction application. *Dalt. Trans.* **2022**, *51*, 15312–15321. [[CrossRef](#)]
71. Cao, C. nan On the impedance plane displays for irreversible electrode reactions based on the stability conditions of the steady-state—II. Two state variables besides electrode potential. *Electrochim. Acta* **1990**, *35*, 837–844. [[CrossRef](#)]
72. Schwab, M.J.; Han, J.; Pfefferle, L.D. Neutral anodic etching of GaN for vertical or crystallographic alignment. *Appl. Phys. Lett.* **2015**, *106*, 241603. [[CrossRef](#)]
73. Hou, X.; Gao, L.; Cui, Z.; Yin, J. Corrosion and Protection of Metal in the Seawater Desalination. *IOP Conf. Ser. Earth Environ. Sci.* **2018**, *108*, 022037. [[CrossRef](#)]
74. Lukatskaya, M.R.; Halim, J.; Dyatkin, B.; Naguib, M.; Buranova, Y.S.; Barsoum, M.W.; Gogotsi, Y.; Lukatskaya, M.R.; Halim, J.; Dyatkin, B.; et al. Room-Temperature Carbide-Derived Carbon Synthesis by Electrochemical Etching of MAX Phases. *Angew. Chemie* **2014**, *126*, 4977–4980. [[CrossRef](#)]
75. Zhou, L.; Bo, B.; Yan, X.; Wang, C.; Chi, Y.; Yang, X. Brief Review of Surface Passivation on III-V Semiconductor. *Catalysts* **2018**, *8*, 226. [[CrossRef](#)]
76. Abdel-Azeim, S.; Sakthivel, S.; Kandiel, T.A.; Kanj, M.Y. Specificity and Synergy at the Oil–Brine Interface: New Insights from Experiments and Molecular Dynamics Simulations. *Energy Fuels* **2021**, *35*, 14647–14657. [[CrossRef](#)]
77. Zaeri, M.R.; Shahverdi, H.; Hashemi, R.; Mohammadi, M. Impact of water saturation and cation concentrations on wettability alteration and oil recovery of carbonate rocks using low-salinity water. *J. Pet. Explor. Prod. Technol.* **2019**, *9*, 1185–1196. [[CrossRef](#)]
78. Feiner, A.-S.; McEvoy, A.J. The Nernst Equation. *J. Chem. Educ.* **1994**, *71*, 493. [[CrossRef](#)]

Disclaimer/Publisher’s Note: The statements, opinions and data contained in all publications are solely those of the individual author(s) and contributor(s) and not of MDPI and/or the editor(s). MDPI and/or the editor(s) disclaim responsibility for any injury to people or property resulting from any ideas, methods, instructions or products referred to in the content.